Springer

KSME

Journal of Mechanical Science and Technology 24 (11) (2010) 2207~2214
www.springerlink.com/content/1738-494x
DOI 10.1007/s12206-010-0807-4

A numerical study on electrohydrodynamic induction pumps using CFD modeling †

Byoung Seo Lee and Joon Sik Lee*

School of Mechanical and Aerospace Engineering, Seoul National University, Seoul, 151-742, Korea

(Manuscript Received July 12, 2009; Revised March 16, 2010; Accepted July 1, 2010)

Abstract

The flow characteristics of EHD induction pumps have been investigated by a numerical method which adds an electric modeling to the conventional CFD. The governing equation for the electric modeling is derived and discretized using the electronic potential as the only dependent variable so that the boundary conditions are satisfied independent of convergence. The numerical results make a good prediction about the frequency-dependent characteristics, which are consistent with both the experiment and the theory. An improvement in understanding the cause of instabilities is achieved to show that the decrement of volumetric force in the local region induces backflow resulting in the instability. The vulnerability was discovered under the conditions of low frequency and large channel depth. The micropump has a maximum flow rate at an optimum channel depth due to the flow instability at larger depths and the flow resistance at smaller one have an undesirable influence upon the one-directionality of flows.

Keywords: EHD; Micropump; Computational fluid dynamics; Frequency dependence; Instability

1. Introduction

With the recent advances in MEMS technology, micropumps have received much attention. The heat rejection problem from high density in microchips requires new cooling methods as an alternative to the conventional cooling systems [1]. Besides, they are needed for a new concept of medical technology [2-4], micro TAS (total chemical analysis), which integrates one or several laboratory functions on a single chip. The micropumps perform their roles as a pump of coolant for microchips and a controller of fluid for micro TAS. Hence, progress in the development of micropumps is important for the growth of the technologies.

The actuators and its working principle have been advanced and renewed in design and fabrication, producing various kinds of micropumps [1, 5, 6]. The micropumps can be divided into the mechanical pump and the non-mechanical pump depending on their driving source. In mechanical micropumps, the displacement type is preferred for restriction on volume and fabrication. It adopts converting the membrane movement to the fluidic motion as the working principle. While the moving components push the fluid directly in mechanical micropumps, the flow in the non-mechanical micropump is generated by electromagnetic force. Since the pumping mechanism of a non-mechanical pump does not include any moving components, they have an advantage in low noise and vibration [7]. In addition, the absence of moving components as in [8] can save the fabrication labors for their relatively simpler design.

The electrohydrodynamic (EHD) micropump is a kind of non-mechanical type. There are the other non-mechanical micropumps such as the electrokinetic pump and magnetohydrodynamic (MHD) pump. EHD micropump is also categorized into the injection type and the induction type. In the injection type, the charges are injected into the fluid from the electrodes and then they are acted on by the Coulomb force between pairs of the opposite electrodes [8]. Each electrode is supplied by a dc current. In the induction type, the charges are generated from the induction phenomena that are caused by the traveling potential wave applied at the electrodes. The electric field (ac fields) at the electrodes itself bring about the flow of the charged fluid by repulsion or attraction. The gradient in electric conductivity or permittivity is needed for the induction. It can be provided by fluid interfaces, inserted particles, or temperature differences. Melcher and Firebaugh [9] fabricated an induction type pump applying temperature differences between the channel walls, and presented a simple theoretic solution. Fuhr et al. [10] succeeded in miniaturizing the pump to the micro-scale with some modifications in design. It is pointed out that the simple theory makes a good

† This paper was recommended for publication in revised form by Associate Editor Yang Na

* Corresponding author. Tel.: +82 2 880 7117, Fax: +82 2 883 0179
E-mail address: jslee123@snu.ac.kr

prediction on the frequency dependence of flows. However, it revealed that the theory cannot be applied to the small channel depth, which induces flow instability. The present study adopted computational fluid dynamics (CFD) to solve the governing equation thoroughly. According to the general governing equation of EHD flows [11, 12], the boundary conditions as shown in the previous research require the iterations to obtain a satisfied solution from assumed boundary value. In this study, the electric potential, of which the boundary condition can be clearly defined, is accepted as the only dependent variable of the electric governing equation, which makes the assumption unnecessary. CFD analysis with a straightforward formulation is conducted on some EHD induction pumps to understand the background for EHD phenomena.

2. Working Principles

The hydrodynamic force in an EHD induction pump is generated by the interaction between the applied electric fields and the induced charges. Induction of charge requires the presence of a spatial gradient in electric conductivity or in permittivity [13]. The gradient in fluid conductivity can be obtained with some treatments. The material interface can act as a source for it [14]. On the other hand, Melcher and Firebaugh [9] developed an EHD induction pump by using the relation between the temperature and the electric conductivity. They used a circulating channel with a straight part in the pumping zone. Its cross section is schematically shown in Fig. 1(a). The difference of temperature between the top wall and the bottom wall, (T_H-T_L), in the pumping zone is kept in order to get the spatial gradient in the electric conductivity as shown in Fig. 1(a). The conductivity increases in the vertical direction since it is a function of temperature. The traveling potential waves acting a force on the induced charge are generated in the array of electrodes imbedded in the top wall. Fuhr et al. [10] fabricated the EHD pump in micro-scale removing the artificial difference in temperature. In their micropump, the electric energy provided by the electrodes, induces the gradient of temperature itself. The electrodes in Fig. 1(b) are reversely placed on the bottom wall as to that in Fig. 1(a).

The conservation of charge presents the equation as follows:

$$\frac{dq}{dt}+\nabla\cdot\boldsymbol{J}=0\,. \tag{1}$$

where q and $\boldsymbol{J}$ are the free charge density and the current density, respectively. Since the fluid velocity is small, the electric conduction is dominant in the current and then the conservation equation can be expressed with the electric field, $\boldsymbol{E}$, as follows.

$$\frac{dq}{dt}+\nabla\cdot(\sigma\boldsymbol{E})=0\,. \tag{2}$$

By the two relations below,

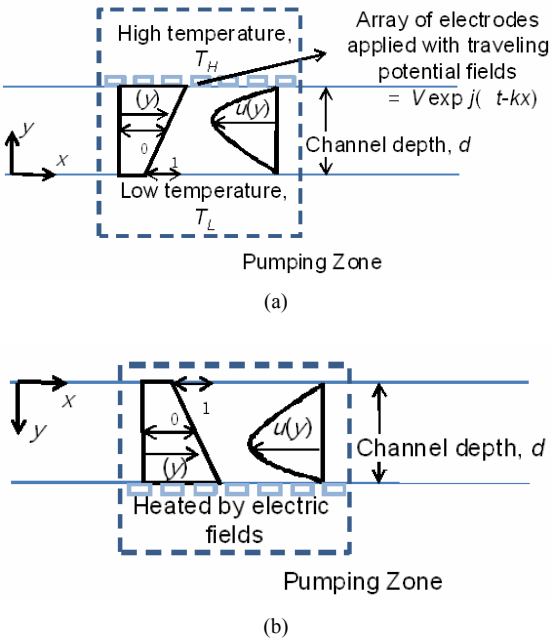

(a)

(b)

Fig. 1. Schematics of EHD induction pump fabricated by (a) Melcher and (b) Fuhr.

$$q=\varepsilon\nabla\cdot\boldsymbol{E}\,, \tag{3}$$

$$\boldsymbol{E}=-\nabla\Phi\,, \tag{4}$$

the governing equation is reduced in relation with potential field, Φ, as the dependent variable to give

$$\nabla(\sigma\nabla\Phi)+\varepsilon(\partial/\partial t)\nabla(\nabla\Phi)=0\,. \tag{5}$$

The boundary condition, applied at the electrode-sided wall, is defined as sinusoidal form as follows:

$$\Phi(x,d,t)=V\exp j(\omega t-kx)\,, \tag{6}$$

Melcher and Firebaugh [9] simplified Eq. (5) in order to solve the EHD induction analytically. The first term in their equation as below neglects the spatial dependence of the electric conductivity accepting the assumption, $\sigma(y)$-σ_0:

$$\sigma_0\nabla^2\Phi+(\sigma_1/d)(\partial\Phi/\partial y)+\varepsilon(\partial/\partial t)\nabla(\nabla\Phi)=0\,. \tag{7}$$

However, the original form Eq. (5) is solved without further assumption in this study. To solve the equation, the dependent variable is divided from the periodic component as to time.

$$\Phi(x,y,t)=\phi(x,y)\exp j\omega t\,. \tag{8}$$

By substituting Eq. (8) for Eq. (5), it results in as below:

$$\nabla(\sigma\nabla\phi)+j\omega\varepsilon\nabla^2\phi=0\,. \tag{9}$$

If the electric conductivity, the order of σ_0, is assumed to be

$\sigma_0\eta(y)$, Eq. (9) is changed to

$$\nabla(\eta\nabla\phi) + jS\nabla^2\phi = 0 , \tag{10}$$

where the dimensionless parameter, S, is defined as $(\omega\varepsilon/\sigma_0)$ according to Melcher and Firebaugh [9]. Eq. (10) results in simpler ones, $\nabla^2\phi = 0$ and $\nabla(\sigma\nabla\phi) = 0$ for two extreme cases in large and small S, respectively. The assumption adopted in a steady term of Eq. (7) can be valid only when S is large enough for the unsteady terms to be dominant over the other terms.

The electric fields induced from the traveling potential waves generate the hydrodynamic force as a form of shear stress in the fluid. The shear stress in continuum media is expressed as follows [15]:

$$\tau_{xy} = \varepsilon E_x E_y . \tag{11}$$

The shear stress averaged over a cycle and the velocity from it are presented by solving Eq. (7) when $1 >> 2kd >> \sigma_1/\sigma_0$ [9].

$$< \tau > = -\frac{(\sigma_1/\sigma_0) S\varepsilon k V^2}{4(1+S^2)d}\zeta^2 , \tag{12}$$

$$u = -\frac{(\sigma_1/\sigma_0) S\varepsilon k V^2}{12(1+S^2)\mu}(\zeta - \zeta^3) , \tag{13}$$

where $\zeta = y/d$. Eq. (13) shows the vertical distribution and the magnitude of the velocity. Especially, the peak velocity at $\zeta = 1/3^{1/2}$ is as given below.

$$u_{\max} = -\frac{(\sigma_1/\sigma_0) S\varepsilon k V^2}{18\sqrt{3}(1+S^2)\mu} . \tag{14}$$

It reveals that the magnitude of velocity has a maximum at S=1 and is in proportion to the voltage squared.

3. Governing equations and numerical methods

The flows in the present study are considered as laminar and incompressible for low velocity and small dimension in EHD flows. The continuity equation and the Navier-Stokes equation are expressed as the governing equations

$$\frac{d\rho}{dt} + \nabla\cdot(\rho\boldsymbol{u}) = 0 , \tag{15}$$

$$\rho\frac{D\boldsymbol{u}}{Dt} = -\nabla p + \nabla\cdot(\mu\nabla\boldsymbol{u}) + \mathrm{S}_{\boldsymbol{u}} , \tag{16}$$

where ρ is density, $\boldsymbol{u}$ is the velocity vectors, p is pressure, and $\boldsymbol{S_u}$ is source term.

The hydrodynamic shear stress is added to a momentum source so that the source terms in the Navier-Stokes equation is changed [12]:

$$\rho\frac{D\boldsymbol{u}}{Dt} = -\nabla p + \nabla\cdot\boldsymbol{\tau} + \nabla\cdot(\mu\nabla\boldsymbol{u}) . \tag{17}$$

It is needed to solve Eq. (9) since Eq. (17) requires the hydrodynamic shear stress. The electric conductivity in Eq. (9) is assumed to be a linear distribution as shown in Fig. 1. Since steady calculation is performed, the shear stress averaged over a period is used in Eq. (17). The potential fields can be obtained by the relation in Eq. (8) and present the force by Eq. (11). All the governing equations are discretized by the finite volume method (FVM), which is the most successful method in CFD. The electric potential equation can be also discretized easily. As already mentioned, it is a kind of diffusion equation whose discretization is a basic part of FVM [16]. The diffusion coefficient is equal to $(\sigma + j\omega\varepsilon)$ in the case. An advantage in using the Eq. (9) is that it prevents the solution from being affected by artificial boundary condition. For example, the boundary conditions of the dependent variables like electric field and charge density in general formulation for EHD governing equations cannot be defined as clearly as that of the potential.

4. Results

Fig. 1 shows the schematics of the pumps and the working principle. They were fabricated and tested by Melcher and Firebaugh [9], and Fuhr et al. [10], respectively. CFD analysis is conducted on the two EHD induction pumps. They are the channels where the flows are driven by traveling potential waves applied to the electrodes. The pumping zone occupies only a part in total channel length. The length of the pumping zone is about $1/k$ for Melcher's and $4/k$ for Fuhr's. The electrodes are imbedded on the top wall of Melcher's and the bottom wall of Fuhr's, respectively. However, it is stressed that the origin of the y coordinate is set across the electrode-sided wall for both cases. The electric conductivity is assumed to be of linear distribution along the depth with the average, σ_0, and the slope, σ_1. In their experiments, corn oil and weak electrolyte-water solution were the working fluids, respectively. The fluid and electro properties in the simulation are set to those of oil and water, most of which are referenced in [9, 10]. The structured meshes 30X200 and 30X300 in flow and depth direction have been adopted for two micropumps, respectively.

4.1 Melcher's pump

According to Melcher's experiments, the channel depth and the wave number are fixed at 3 cm and 7.08 m^{-1}, respectively. Various frequencies and voltages have been simulated for testing their effect on flow characteristics. The linear distributions of the electric conductivity and viscosity were given in the y direction by their dependence of temperature. Fig. 2 shows the variation of maximum velocity generated in the pumping zone due to the applied peak voltages. The frequency was set to 0.4 Hz, a theoretical optimum frequency (S=1, [9]).

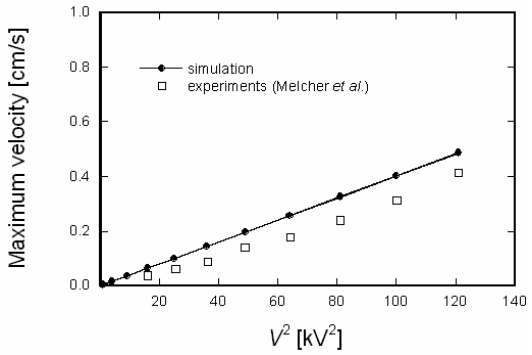

Fig. 2. Maximum velocity vs. applied voltage (at constant frequency : 0.4 Hz).

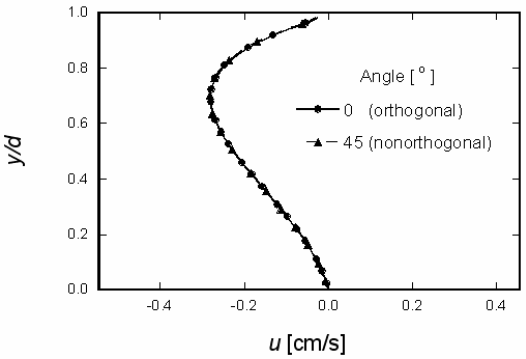

Fig. 3. Velocity profiles for orthogonal and nonorthogonal grids (at 2.0 Hz).

It shows a good agreement with the experiments. In addition, the simple analysis resulting in Eq. (14) supports the present linear relationship between the magnitude of the velocity and the amplitude squared of potential. This also proves that the present computer program has been well-developed. The other validation in the present study is in relation to the applicability to general coordinates. Fig. 3 presents the velocity profiles in the pumping zone calculated from orthogonal girds and nonorthogonal grids. The orthogonal grid system consists of rectangular meshes. The computation is conducted under the potential waves of 2.0 Hz and 11 kV. The parallelograms with angle of 45° are adopted as nonorthogonal grids. Despite the large difference in angle, they have nearly the same solutions. From this, the method adopted in this study is concluded to be successful in application to more complex geometry using nonorthogonal grids.

Next, the effect of frequency at constant peak potential, V=11 kV, is investigated. Fig. 4 shows the velocity profiles made by four different frequencies. The maximum in the velocity profile was the highest at the frequency of 0.6 Hz, which is rather larger than the theoretic value, 0.4 Hz. According to the analysis of Melcher and Firebaugh [9], the pump has the highest velocity levels when S is unity. Despite the small difference in the optimum frequency, it is common in both the present and the experiment that the absolute velocity decreases with deviation from the optimum frequency. As

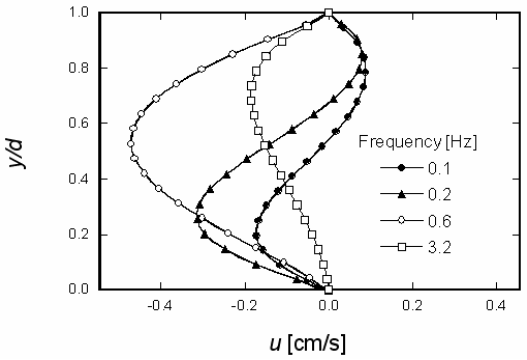

Fig. 4. Velocity profiles for various frequencies (at V = 11 kV).

expected, the simulation results show the decrease in the absolute velocity for the other three cases (0.1, 0.2, and 3.2 Hz). However, it is beyond what the simple analysis can predict. The diversity of the shape in the velocity profile is an example. Eq. (13) obtained from the simple analysis presents the same shapes of velocity- 3rd order polynomial function, independent of the frequency. Contrary to it, the present profiles show that the position of maximum velocity shifts from the bottom to the top with increase in the frequency. At a low frequency of 0.1 and 0.2 Hz, flow instability is observed such as backflow and separation. The presence of instability at low frequency is overlooked by the simple analysis but reported by the experiments. The reason that the simple analysis cannot account for the instability is that its assumption is not valid for larger frequency region (S > 1) as already referred in Section 2. They show similar profiles with the theoretic one only when S is large enough as in frequency of 3.2 Hz. The shape that has a maximum near the top wall is similar to the one by Melcher's. In lower frequency, the points are reversely shifted even to include a certain instability, which is aligned with the experiments. The experiments have shown instabilities below 0.1 Hz.

The cause of the instability can be described by comparing the distributions of the electric potential as shown in Fig. 5. The distributions in Fig. 5(a) indicate the electric potential at an instant. With time, it moves in the x direction. At y=d, they all have the sinusoidal form by the boundary condition given by Eq. (6). The magnitude of the signal attenuates with the decrease of y in different ways for three frequencies. Fig. 5(b) shows the profiles at the valley of the potential in the y direction. In a large frequency of 2.4 Hz, the potential energy decreases linearly with the depth direction. As the frequency increases, the profile is modified to be of parabolic form. The lower slope of low frequency near the top wall influences the shear stress distribution. The shear stress in Fig. 6 shows a clear parabolic distribution at the highest frequency of 3.2 Hz as suggested by Eq. (12). As the frequency decreases, the parabolicity is defected from the top wall. It is supposed to be related to the low slope of potential pointed out in Fig. 5. Given that the variation of shear stress in the x-direction is negligible, the volumetric force acted by the shear stress can be considered as below:

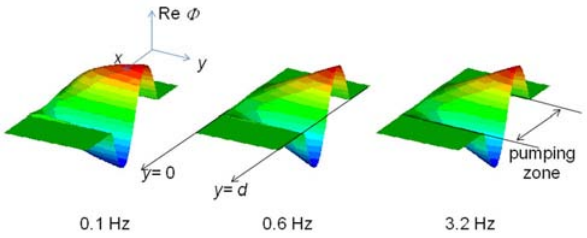

(a) In *xy* plane

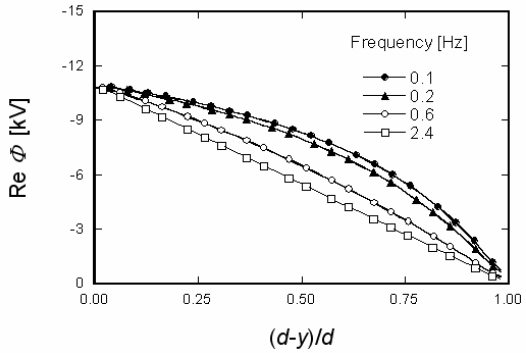

(b) In depth direction

Fig. 5. Distribution of electric potential.

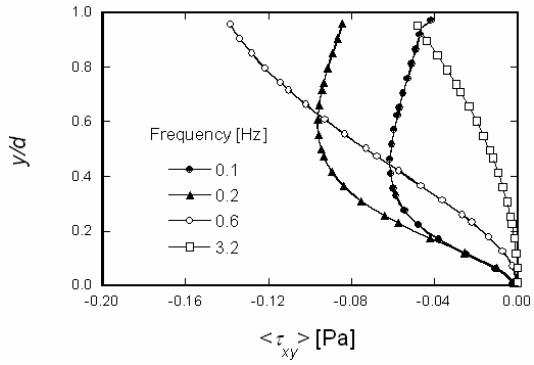

Fig. 6. The shear stress profiles for various frequencies.

$$f_v = \nabla \cdot f_s \approx \partial \tau_{xy} / \partial y \,. \tag{18}$$

It is clear that the reversed slope of 0.1 and 0.2 Hz near the top wall acts as a source for backflow. The slopes show that the fluid in the upper channel is acted on by a volumetric force in the reverse direction.

4.2 Fuhr's micropump

Fuhr et al. [10] miniaturized the Melcher pump. The channel depths which are orders of ten or hundred μm, are tested. With this, some other modifications are realized in the design as already mentioned. The traveling waves are used with higher frequency (100 kHz~30 MHz) and smaller voltages (20 V~50 V). The wave number is increased to 3×10^4 m^{-1} in proportion with the miniaturization. The total channel length is 4 mm.

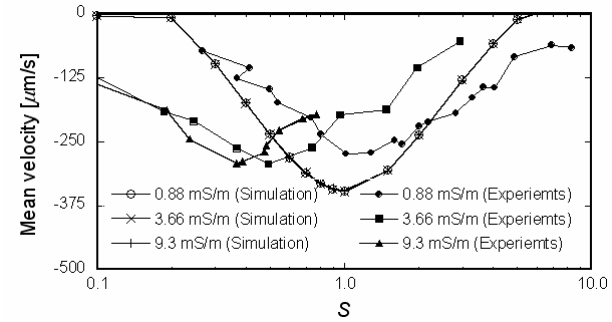

Fig. 7. Frequency dependence of mean flow velocity.

First, the frequency-dependency is investigated by comparing the simulation with the experiments. The voltage is fixed at 50 V. Fig. 7 shows the variation of mean velocity as to dimensionless frequency, $S = (\omega\varepsilon/\sigma_0)$. The simulation results for three average electric conductivities show nearly the same mean velocity as to dimensionless frequency. They all have their maximum velocities at $S = 1$. Although this tendency is coincident with Melcher's analysis as mentioned above, the optimum frequency in the experiments decreased from $S = 1$ with the increase in electric conductivity. However, they are in common that the flow rate decreases with deviation from a certain optimum frequency.

Fuhr et al. report the upper limit in the channel depth. According to them, flow instability occurs above the depth but the increase in $2kd$ prevents the theoretic interpretation. For this, a parametric study on the channel depth is conducted. The channel depths for 20~200 μm are simulated to present the velocity profiles as in Fig. 8. The net flow is in the negative direction, contrary to the traveling wave. Each profile has its separation point due to backflow. The point moves from the upper wall (y=0) to the electrode sided wall (y=d) as the channel depth increases. That is, the instability increases with channel depth. Therefore, the present simulation based on CFD can be supposed to succeed in simulating the instability induced by the depth. The electric potential energy is shown in Fig. 9 as in Section 4.1. The distribution is in the reverse y direction. It can be the attenuation of amplitude in the direction. At 20 μm, the amplitude linearly decreases with a constant slope. At other depths, the slope varies with the y direction. Above 100 μm, the electric fields cannot reach nor affect the top region (near y=0). Hence, it is difficult for the region to be pumped. Fig. 10 shows the profiles of the shear stress that generates the pumping force. The micropump with 20 μm channel depth has parabolic distribution in shear stress as supported by Eq. (12) of simple theory. However, the larger depths shift the origins of the stress profiles. The shear stress is kept zero in the electric fields-free region as previously mentioned. Eq. (18) proves that the pumping force in the region is extremely small. In conclusion, the instability is related to the limit in the penetration depth of the electric fields. The

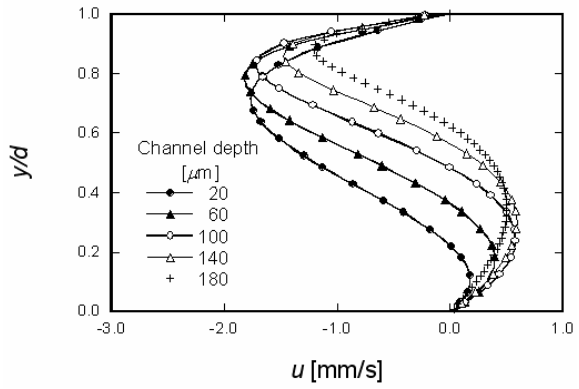

Fig. 8. The velocity profiles for various channel depths.

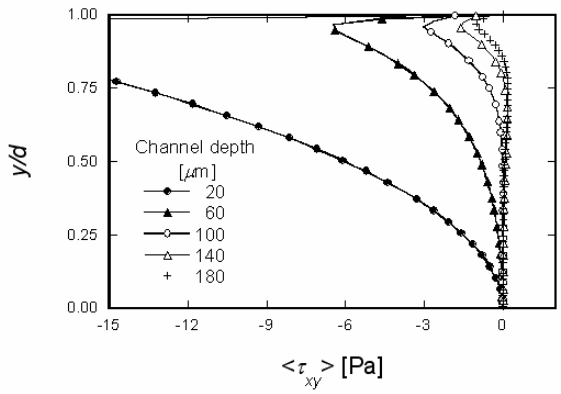

Fig. 10. The shear stress profiles for various channel depths.

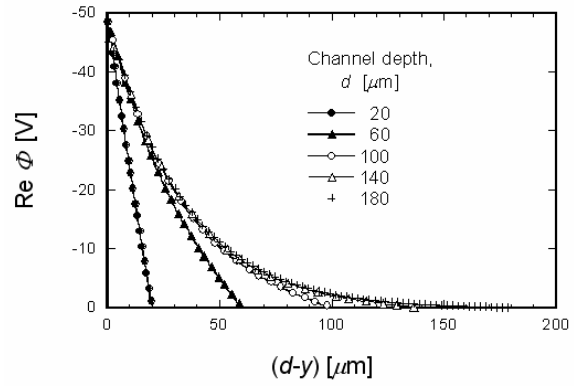

Fig. 9. The distribution of electric potential in the depth direction.

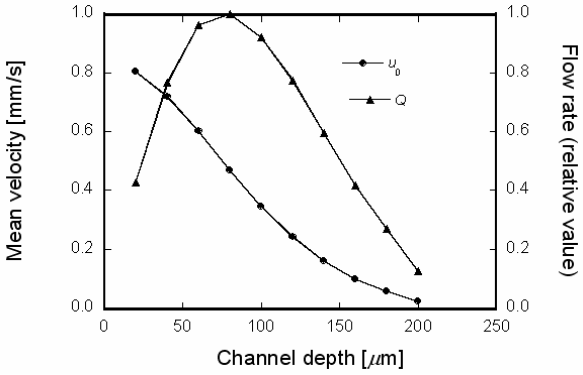

Fig. 11. The variation of velocity and flow rate depending on channel depths.

penetration depth of sinusoidal waves is about 50~100 μm as inferred from Fig. 9. If the channel depth exceeds the penetration depth, the region cannot be pumped so that it results in flow instability.

The two instabilities show three differences between Melcher's and Fuhr's, which can be summarized as follows.

(1) The external condition: low frequency in Melcher's and large depth in Fuhr's.

(2) The distribution of potential waves in the depth direction: the attenuation of the amplitude is apparent near the opposite side to the electrode at Melcher's instability, but the fields cannot reach the region far from the electrode at Fuhr's instability.

(3) The distribution of shear stress: the theoretic distribution of Eq. (12) is terminated at the electrode side in Melcher's but it starts from the field-affected region in Fuhr's.

Finally, the performance of the micropump is investigated in relation to the mean velocity and the flow rates. The flow rates indicate the pumping capacity of the pumps. The increase in the depth diminishes the velocity under the direct influence of the flow instability. It shows monotonic decreases in Fig. 11. However, small channel depth itself has the deterministic shortcomings in micro scaled applications. It is that it has larger flow resistance for same flow rates. Therefore, it has a certain optimum depth, at $d \approx 80$ μm, about the flow rates as shown in Fig. 11. The upper limit is constrained to the flow instability and the lower the flow resistance.

5. Conclusions

A numerical program based on CFD has been developed especially to describe EHD induction pumps. In the numerical formulation on electric phenomena, the potential is adopted as the only dependent variable to exclude some assumptions about boundary conditions. The present study verified its applicability on the generalized coordinates. The simulations were conducted on the two pumps of Melcher's and Fuhr's to present the conclusions as follows.

As to the dependence of the frequency, they show a good agreement with the simple analytical solution as well as the experiment. The velocity has the maximum near the dimensionless frequency, $S = 1$. If the frequency increases or decreases from it, the drop in velocity is shown. However, there are discrepancies between the simulation and the experiments. The deviation of the optimum dimensionless frequency from unity, which is observed in Fuhr's experiment, is a representative example.

The present simulations make it possible to offer a theoreti-

cal background for the instabilities in EHD induction pumps, which cannot be described by the simple theory. It is shown that the instability is related to the distribution of electric potential. The backflow motions take place where the amplitude of potential has a steep slope. It results in the reduction in volumetric force due to shear stress, the driving force in EHD induction pumps. The differences of the instability are clarified between Melcher's and Fuhr's. Especially, the instability in Fuhr's is induced by reducing the penetration depth that the potential can reach. Fuhr's micropump has a certain optimum channel depth for flow rates, because the flow is interrupted by the instability of a large depth and by the resistance of a small depth.

Acknowledgment

This work was supported by the Micro Thermal System Research Center, Seoul National University, sponsored by the Korean Science and Engineering Foundations.

Nomenclature

d : Channel depth
E : Electric field
$\boldsymbol{E}$: Electric field vector
fs : Surface force
fv : Volumetric force
$\boldsymbol{J}$: Current density vector
k : Wave number
p : Pressure
q : Free charge density
Q : Flow rate
S : Dimensionless frequency
$\boldsymbol{S_u}$: Source terms in momentum equation
t : Time
T_H : High temperature
T_L : Low temperature
x, y : Spatial coordinates
u : Velocity in the x direction
$\boldsymbol{u}$: Velocity vectors
V : Voltage

Greeks Symbol

ε : Permittivity
ζ : Dimensionless parameter (=y/d)
η : Unit function
μ : Viscosity
ρ : Density
σ : Electric conductivity
$\boldsymbol{\tau}$: Shear stress
ϕ : Time-independent electric potential
$\boldsymbol{\Phi}$: Electric potential
ω : Angular velocity

Superscript

$\langle\rangle$: Cycle averaged value

Subscript

0 : Average value
1 : Slope of linear function

Abbreviation

CFD : Computational fluid dynamics
EHD : Electrohydrodynamic
FVM : Finite volume method
MHD : Magnetohydrodynamic

References

[1] V. Singhal, S. Garimella and A. Raman, Microscale pumping technologies for microchannel cooling systems, *Appl. Mech. Rev.* 57 (3) (2004) 191-221.
[2] P. Tabeling, *Introduction to microfluidics* (translated ed.), Oxford University Press, New York, USA (2005).
[3] N.-T. Nguyen and S. T. Wereley, *Fundamentals and applications of microfluidics*, Artech House, Boston, USA (2006).
[4] A. Manz, N. Graber and H. M. Widmer, Miniaturized total chemical analysis systems: a novel concept for chemical sensing, *Sens. & Actu. B* 1 (1-6) (1990) 244-248.
[5] N.-T. Nguyen, X. Huang and T. Chuan, MEMS-micropumps: a review, *J. of Fluid Eng.* 124 (2) (2002) 384-392.
[6] H. Yoshida, The wide variety of possible applications of micro-thermofluid control, *Microfluidics and Nanofluidics* 1 (4) (2005) 289-300.
[7] W.-S. Seo, S.-Y. Yang, B.-R. Lee, K.-K. Ahn and Y.-B. Ham, Design, fabrication and experimental investigation of a planar pump using electro-conjugate fluid, *J. of Mech. Sci. and Tech.* 21 (8) (2007) 1320-1327.
[8] A. Richter, A. Plettner, K. A. Hofmann and H. Sandmaier,.A micromachined electrohydrodynamic (EHD) pump, *Sens. and Actu. B* 29 (1-3) (1991) 159-168.
[9] J. R. Melcher and M. S. Firebaugh, Traveling-wave bulk electroconvection induced across a temperature gradient, *Phys. of Fluids,* 10 (6) (1967) 1178-1185.
[10] G. Fuhr, R. Hagedorn, T. Müller, W. Benecke and B. Wagner, Microfabricated electrohydrodynamic (EHD) pumps for liquids of higher conductivity, *J. of MEMS* 1 (3) (1992) 141-146.
[11] A. Castellanos, Chap. 3 Mechanical equations, *Electrohydrodynamics* (edited by A. Castellanos), Springer, New York, USA (1998) 54-56.
[12] J. Darabi and C. Rhodes, CFD modeling of an ion-drag micropump, *Sens. and Actu. A* 127 (1) (2006) 94-103.
[13] S. F. Bart, L. S. Tavrow, M. Mehregany and J. H. Lang, Microfabricated electrohydrodynamic pumps, *Sens. and Actu.* A 21 (1-3) 1990 193-197.
[14] J. F. Hoburg and J. R. Melcher, Internal electrohydrodynamic instability and mixing of fluids with orthogonal field

and conductivity gradients, *J. of Fluid Mech.* 73 (1976), 333-351.
[15] J. A. Stratton, *Electromagnetic theory*, McGraw-Hill, New York, USA (1941).
[16] S. V. Patankar, *Numerical heat transfer and fluid flow*, Taylor & Francis, Washington, USA (1980).

Byoung Seo Lee obtained a Ph. D in the Mechanical engineering department, Seoul National University, Korea, in 2005. As a postdoctoral researcher in Micro Thermal System Laboratory, Seoul National University, he has been concerned with microscale heat transfer, CFD analysis in the complex geometry, and microfluidics.

Joon Sik Lee received his B. S and M. S degrees in Mechanical Engineering, Seoul National University, and his Ph.D. from U.C. Berkeley. His research interests are in micro/nanoscale heat transfer, thermal process design, and gas turbine heat transfer. Currently, he is the director of the Micro Thermal System Research Center, Seoul National University.